Additive Manufacturing 77 (2023) 103798

Contents lists available at ScienceDirect

Additive Manufacturing

journal homepage: www.elsevier.com/locate/addma

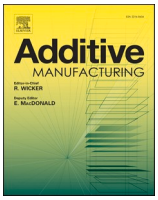

Synchrotron validation of inline coherent imaging for tracking laser keyhole depth

Tristan G. Fleming [a,d,*], Samuel J. Clark [b], Xianqiang Fan [c,d], Kamel Fezzaa [b], Chu Lun Alex Leung [c,d], Peter D. Lee [c,d,**], James M. Fraser [a,***]

[a] Department of Physics, Engineering Physics & Astronomy, Queen's University, Kingston, Ontario K7L 3N6, Canada
[b] X-ray Science Division, Argonne National Laboratory, 9700 S Cass Ave, Lemont, IL, USA
[c] Department of Mechanical Engineering, University College London, WC1E 7JE, UK
[d] Research Complex at Harwell, Rutherford Appleton Laboratory, Harwell, Didcot OX11 0FA, UK

ARTICLE INFO

Keywords:
Laser keyhole welding
Synchrotron X-ray imaging
Inline coherent imaging
Optical coherence tomography

ABSTRACT

In situ monitoring is critical to the increasing adoption of laser powder bed fusion (LPBF) and laser welding by industry for manufacture of complex metallic components. Optical coherence tomography (OCT), an interferometric imaging technique adapted from medical applications, is now widely used for *operando* monitoring of morphology during high-power laser material processing. However, even in stable processing regimes, some OCT depth measurements from the keyhole (vapor cavity formed at laser beam spot) appear too shallow or too deep when compared to *ex situ* measurements of weld depth. It has remained unclear whether these outliers are due to imaging artifacts, multiple scattering of the imaging beam within the keyhole, or real changes in keyhole depth, making it difficult to accurately extract weld depth and determine error bounds. To provide a definitive explanation, we combine inline coherent imaging (ICI), a type of OCT, with synchrotron X-ray imaging for simultaneous, *operando* monitoring of the full 2-dimensional keyhole profile at high-speed (280 kHz and 140 kHz, respectively). Even in a highly turbulent pore-generation mode, the depth measured with ICI closely follows the keyhole depth extracted from radiography (>80% within ± 14 μm). Ray-tracing simulations are used to confirm that the outliers in ICI depth measurements (that significantly disagree with radiography) primarily result from multiple reflections of the imaging light (57%). Synchrotron X-ray imaging also enables tracking of bubble and pore formation events. Pores are generated during laser welding when the sidewalls of the keyhole rapidly (>10 m/s) collapse inwards, pinching off a bubble from the keyhole root and resulting in a rapid decrease in keyhole depth. Evidence of bubble formation can be found in ICI depth profiles alone, as rapid depth changes exhibit moderate correlation with bubble formation events (0.26). This work moves closer to accurate, localized defect detection during laser welding and LPBF using ICI.

1. Introduction

Inline coherent imaging (ICI) is a low-coherence interferometric imaging technique, similar to optical coherence tomography (OCT), that has been successfully deployed in several laser material processing applications including laser welding, micromachining, and laser powder bed fusion (LPBF) additive manufacturing [1,2]. ICI is uniquely suited to these processes due to its robustness to intense process emissions, which include broadband blackbody radiation and metal vapor jet formation. Photodiode measurements of these emissions, while simpler to integrate into LPBF machines or laser welding cells, are susceptible to material-dependent changes in the emissions (blackbody radiation, plasma, etc.) from the keyhole/melt pool [3]. ICI captures depth measurements at high-speed from the keyhole during laser welding and LPBF. The keyhole (or vapour depression) depth, which corresponds closely with the penetration depth of the LPBF track or weld, is a key indicator of process quality. An LPBF track needs to penetrate the previously deposited layer(s) to avoid "lack-of-fusion" defects [4]. To

* Corresponding author at: Department of Physics, Engineering Physics & Astronomy, Queen's University, Kingston, Ontario K7L 3N6, Canada.
** Corresponding author at: Department of Mechanical Engineering, University College London, WC1E 7JE, UK.
*** Corresponding author.
E-mail addresses: tristan.fleming@queensu.ca (T.G. Fleming), peter.lee@ucl.ac.uk (P.D. Lee), james.fraser@queensu.ca (J.M. Fraser).

https://doi.org/10.1016/j.addma.2023.103798
Received 9 April 2023; Received in revised form 21 September 2023; Accepted 23 September 2023
Available online 26 September 2023

increase build rate, LPBF is often performed at high velocity (~1 m/s), resulting in a "pedestal" shaped keyhole with a wide keyhole opening (>laser beam diameter) [5]. By contrast, laser welding is often performed at lower velocity (<100 mm/s) to achieve deep penetration, which results in a high aspect-ratio keyhole and increased likelihood of keyhole porosity [6]. Additionally, high velocities are also increasingly being used for laser battery tab welding [7]. In this case, insufficient weld penetration can increase electrical resistance and reduce battery performance, while over-penetration can damage the battery itself [8].

Before this work, *operando* ICI depth measurements from a keyhole have only been corroborated by *ex situ,* destructive microscopy [1], which says little about the accuracy of ICI for tracking keyhole dynamics. While ICI depth measurements largely agree with the fusion region in micrographs, there are still a significant number of outliers that do not agree and cases when ICI experiences completely signal loss ("dark" measurement). A better understanding of the keyhole morphologies that result in outlying and dark ICI depth measurements could improve the accuracy of ICI-based depth-tracking compared to *ex situ* measurements. It could also provide more information about the keyhole dynamics, which are not observable *ex situ* from static, cooled, and mechanically sectioned samples.

One possible cause of outliers is multiple reflections of the imaging beam within the keyhole. Rather than reflecting off the keyhole root and then exiting through the top of the keyhole, the ICI beam can reflect off the keyhole sidewalls. Multiple reflections are key to efficient energy coupling between the processing beam and the (highly reflecting) metal [9] but have the potential to obscure measurement. Depending on the tilt of the keyhole walls and the transverse position of the ICI beam [10], the ICI beam can be reflected across and out of the keyhole (too shallow) or reflected down towards the keyhole root where it can undergo several more reflections within the cavity (too deep). As they result in deviations from the true keyhole depth, efforts have been made to eliminate multiple reflections along with noise from other sources like speckle.

Smoothing of OCT data is often based on frame-averaging or machine learning [11–13]. Recently, Boley et al. developed a denoising algorithm and percentile filter for analyzing OCT depth measurements from deep penetration (1–4 mm) laser welding [14]. Time-windowed (5–50 ms) measurements filtered based on frequency (i.e., rarely measured depths are discarded) and statistical distribution showed excellent agreement with *ex situ* microscopy. Such an approach improves correlation with final part structure but at the cost of reduced effective imaging rate and exclusion of transient dynamics. More importantly, without real-time, experimental verification of the 2D keyhole geometry, it is impossible to quantify the importance of multiple reflections or discern them from true outliers in OCT depth measurements (whether caused by noise or real sporadic depth increases such as observed in LBPF raster scanning [15]).

The causes of signal loss in OCT of laser keyhole welding have also remained elusive. For high aspect-ratio and unstable keyholes, like those that form when welding high-reflectivity metals (e.g. Al, Cu), at high oxygen levels, or without proper assist gas, OCT may go dark > 90% of the time [16]. Our previous work suggests that this is mostly due to geometric signal loss, i.e. the keyhole geometry backreflecting the ICI beam outside the collection angle of the ICI system. Motion artifacts and speckle could also contribute to loss but are difficult to measure. Since the ICI beam is spatially coherent, it is susceptible to speckle loss from variations in sample morphology over the length scale of the imaging wavelength (864 nm here) [17].

Though limited to very specific part geometries, high-speed synchrotron X-ray imaging is uniquely capable of verifying ICI of laser keyhole welding and LPBF. By directly imaging the keyhole geometry in 2D, X-ray imaging offers new insights into the source of outliers and complete signal loss in simultaneous ICI depth measurements. X-ray imaging also allows for correlation of bubble and pore formation events with features of the ICI depth data, aiming to classify and predict porosity defects using ICI. The fast dynamics of the process and large amount of *in situ* data for each pore formation event make feature extraction challenging.

Recently, Paulson et al. trained a machine learning (ML) algorithm with simultaneous, *operando* (during laser processing) infrared and synchrotron X-ray imaging data [18]. They were able to accurately predict whether significant porosity would form within an LPBF track over different processing regimes but found too much scatter in the thermal histories over smaller segments (<100 ms) of each track. This prohibited localized detection of pore formation. Over multiple segments, thermal histories with high peak temperatures, and non-monotonic cooling (dips and increases in temperature after the laser pass) were correlated with porosity formation. Based on modelling of keyhole dynamics [19–21], the corresponding keyhole depth signatures are likely to include spiking and collapse.

The time scales of spiking and collapse are of key importance to understanding the temporal resolution required for tracking dynamics. Recent work in acoustics-based monitoring found that the most informative features for classifying pore formation events was the spectral power in the 20–50 kHz frequency band [22–25]. This agrees with work by Khairallah et al. [26] that used ultrahigh-speed (25 MHz) integrating sphere radiometry measurements of keyhole absorptivity, coupled with synchrotron X-ray imaging, to uncover fast, periodic oscillations (~40–50 kHz) in the keyhole for ~1 ms leading into a pore generation mode. In the pore generation mode, the authors observed turbulent multi-modal oscillations in the keyhole, spanning frequencies of 20 kHz to > 60 kHz. The Nyquist limit for resolving keyhole dynamics during pore formation is then at least 40 kHz.

In this paper, an ICI system is integrated into the LPBF test rig at the Advanced Photon Source (APS) (Section 2.1, detailed in [27]) to capture depth measurements from laser keyhole welding of aluminum alloy 6061 *operando* and simultaneous with synchrotron X-ray radiography of the 2D keyhole shape. High-speed synchrotron X-ray imaging provides real-time verification of ICI for tracking fast keyhole dynamics. By simultaneously capturing the full 2D keyhole morphology, radiography can also improve our understanding and handling of outliers in ICI data, when ICI significantly disagrees with X-ray. In particular, it can discern the prevalence and impact of multiple reflections of the imaging beam within the keyhole, a lasting mystery in OCT monitoring of laser keyhole welding and LPBF.

2. Materials and methods

The experimental set-up consisted of: the LPBF test rig in-house at the beamline (detailed in [27]); a linear motion stage for translating the sample and imaging in a Lagrangian frame of reference; an interferometric, inline coherent imaging (ICI) system for high-speed, *in situ* and *operando* morphology measurements; and the synchrotron X-ray beamline, 32-ID at APS, used to capture *in situ* and *operando* radiographs.

2.1. Laser powder bed fusion

Laser powder bed fusion (LPBF) was carried out using an ytterbium fiber laser (IPG YLR-500-AC, IPG Photonics, Oxford, Massachusetts, USA) with a nominal wavelength and maximum power of 1070 nm and 520 W, respectively. Since the laser beam is redirected by the ICI imaging module (Section 2.2), the height of the laser focal plane was remeasured for this study (Section A.1). Based on this measurement, the spot size of the laser beam at the substrate surface was set to be 47 ± 2 μm ($1/e^2$ diameter). This was chosen to be slightly larger than the beam waist to increase the keyhole width. Generally, ICI alignment is easier and more backscattered imaging light can be collected from wider keyholes. As discussed in Section 2.2, the nominal laser power was limited to a maximum of 260 W due to the power-handling limitations of the dielectric mirror. Based on a laser power calibration done at APS in 2019 and accounting for losses of 3% and 0.8% at the dichroic and

dielectric mirror, respectively, the expected power at the substrate is 253 ± 1 W (± 0.5% typical stability [28]).

While making important contributions to the field, previous X-ray imaging studies using a galvanometric scanner have been limited in total imaging time by the field-of-view (FOV) (Section 2.3). Longer imaging times are needed for high-resolution frequency analysis, of keyhole depth for example, and for imaging of AM at higher scan speeds and of larger components. By instead using a linear motion stage (Parker MX80L) to translate the sample, keeping the laser stationary, X-ray imaging time is only limited by camera memory. This allowed us to increase the imaging time of the APS system from 2 ms (280 frames, 1 mm track length) to 14 ms[1] (1260 frames, last ~7 mm of each ~9.5 mm track) for the frame rate (140 kHz) and scan speed (500 mm/s) used here. Traverse rate was held constant at 510 ± 6 mm/s for this study, confirmed using ICI (Section A.2).

The substrates used in this study were aluminum 6061 (McMaster-Carr, cold-rolled) with dimensions ($l \times h \times t$): 49 ± 1 × 10.0 ± 0.1 × 1.00 ± 0.02 mm (thermophysical properties listed in Table S 2). The relevant energy densities are given in Table 1.

While aluminum 6061 is a widely used material, especially in structural applications due to its high strength-to-weight ratio, it is also sensitive to solidification cracking during LPBF [31] or laser welding [32]. Like many aluminum alloys, it also has a number of properties that increase the likelihood of pore formation [33]. The use of aluminum 6061 in LPBF has thus been quite limited. However, the high frequency of porosity and cracking defects during LPBF of aluminum 6061 can be beneficial for imaging and understanding the dynamics of pore or crack formation.

Simultaneous X-ray and ICI imaging results from LPBF, with a layer of powder, will be presented in future work. Previous work by Bitharas et al. using synchrotron X-ray imaging suggests the variations in weld depth with and without powder are similar, but also noted a slight decrease in penetration depth and irregularly shaped keyholes in the presence of powder [34]. ICI of metal powder layers, including *in situ* LPBF, is characterized by broader A-line peaks due to the sampling of the powder particle(s) surface height within the imaging spot size, and somewhat reduced peak backscattered intensity due to diffuse reflection, as detailed in our previous work [2,35].

2.2. Inline coherent imaging

The substrate holder, linear motion stage and ICI optics are depicted in Fig. 1. The substrate holder is fastened to the linear motion stage, which is mounted into the chamber of the LPBF test rig.

The ICI system is based around a single-mode fiber-coupled, broadband superluminescent diode light source (BLM2D series, Superlum, 864 ± 37 nm), which is split into two free-space interferometer arms ("reference" and "sample", reference has fixed path length), and a high-speed spectrometer [2]. For fast computation, spectral interferograms recorded by the high-speed spectrometer are processed using a homodyne filtering technique similar to a fast Fourier transformation, as described by Webster et al. [36]. The system is characterized by an axial point spread function of 6 μm, measured experimentally and matching the theoretical value based on the bandwidth of the imaging light source [37]. The focused spot size of the imaging beam was measured to be 25 ± 4 μm ($1/e^2$).

The optics in the sample arm of the ICI system (Fig. 1) are as follows: (1) ICI scanning module consisting of a micro-electromechanical systems (MEMS) scanner mirror mounted to one of the external ports on the LPBF test rig, and (2) ICI imaging module mounted inside the chamber and consisting of a focusing lens, a dichroic mirror (Edmund Optics 86–688), and a final dielectric mirror (Thorlabs BB1-E03). The MEMS scanner allows for alignment of the imaging beam to the high-power laser beam. The imaging beam is coupled from the scanning module into the chamber where it is focused, combined coaxially with the laser beam at the dichroic mirror, and directed towards the sample by the dielectric mirror.

Alignment of the ICI beam to the processing laser was achieved by marking vertical and horizontal lines onto a staircase calibration substrate using the laser. The staircase calibration substrate included five planes (the nominal substrate height, ± 0.5 mm, and ± 1 mm) to align the two beams through the laser focus. After marking a line, the ICI beam was raster scanned across it while adjusting either the final mirror in the ICI scanning module or the dichroic mirror in the ICI imaging module to center the height signature from the marked line in the raster scan (positioning the line at the home position of the MEMS scanner). This was repeated for the orthogonal direction (vertical and horizontal lines). For high-speed moving welds and LPBF tracks, the transverse position of the keyhole root is slightly displaced from the laser beam. The ICI beam was then strategically offset to trail the laser by 10 μm using the MEMS scanner. This offset was found to maximize the average ICI backscattered intensity for the selected process parameters by centering the ICI beam on the keyhole root rather than partway along the front keyhole wall. This offset of the keyhole root behind the laser beam position during high velocity LPBF has been previously observed [5].

An individual ICI measurement, referred to as an axial line or "A-line", yields backscattered intensity as a function of depth over the measurement range (Fig. S6) [2]. A flat interface in the sample arm yields a single peak in the A-line corresponding to the point spread function of the imaging system. A single depth value can be extracted from each A-line using several different methods. For fast processing, the depth bin with the maximum backscattered intensity is used (maximum intensity tracking) after first applying a threshold to avoid errors due to background noise (see Section 3.4). A noise threshold of 13 dB was applied when processing the ICI data presented in Fig. 2 and Fig. 3. The final step in ICI data processing is decimation, for example, maximum intensity tracking but over blocks of successive A-lines, with the aim of improving tracking accuracy (see Section 3.4). Note that no decimation was applied when processing the ICI data presented in Figs. 2 and 3.

Due to the proximity of the optics to the laser focus, power handling needed to be considered. Firstly, damage to the dichroic mirror occurred at nominal laser powers above 260 W, which was set as the limit for this study. Secondly, the stability of the ICI optics during laser processing was verified prior to conducting experiments by positioning a beam dump underneath the laser and a silver mirror next to it. The ICI beam was directed at the silver mirror while firing the laser and height measurements were captured. This way, the effects of thermal expansion/contraction or deformation of the dichroic or dielectric mirrors due to the laser would be included in the ICI height measurements of the silver mirror. Gaussian fitting of A-lines was performed instead of maximum intensity tracking as described above, which is more intensive, but can track the centroid of the A-line peak, and corresponding height, over time with sub-micron precision. Over 20 ms of laser on-time, the mirror

Table 1
Calculated energy density parameters for aluminum alloy 6061 with a laser power of (253 ± 1) W, $1/e^2$ beam diameter of 47 ± 2 μm and scan speed of 510 ± 6 mm/s.

Energy density parameter	Value	Uncertainty
Linear energy density (LED) [J/mm]	0.496	0.006
Area energy density (AED) [10^3 J/cm^2]	1.05	0.05
Normalised enthalpy[29]	18	1
Normalised enthalpy product[30]	29	1

[1] 19 ms laser on time less 5 ms for the slow X-ray shutter on the beamline to completely open

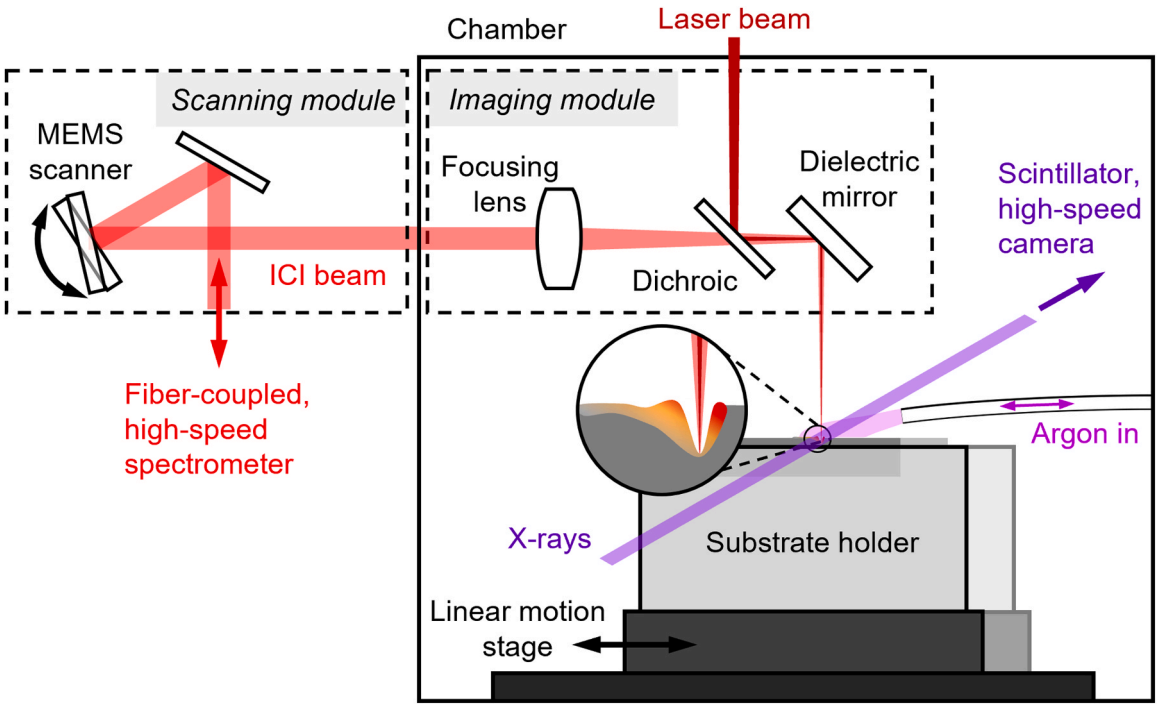

Fig. 1. Simultaneous *operando* X-ray and inline coherent imaging (ICI) of LPBF-AM process. Schematic of experimental set-up integrated into LPBF test rig including an ICI scanning module mounted to one of the viewing ports on the chamber and an ICI imaging module mounted inside the chamber above a linear motion stage and custom substrate holder.

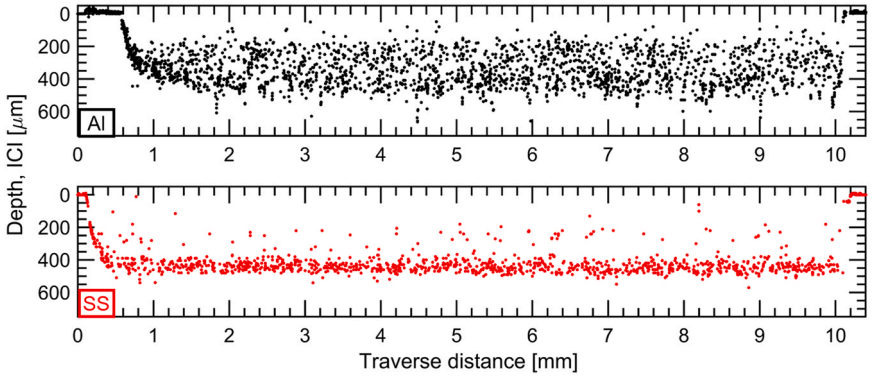

Fig. 2. ICI measured depth profile using maximum intensity tracking (relative to the substrate) from a ~10 mm long line weld on aluminium alloy 6061 (top), stainless steel 316 L (bottom). Mean and standard deviation in depth over 1–9 mm is 352 μm and 105 μm, and 431 μm and 57 μm for Al and SS respectively. Line welds were written using the laser workstation (SupplementaryAA.3) with parameters: 872 W and 150 mm/s (Al), and 463 W and 150 mm/s (SS). The laser turns on at a traverse distance of 100 μm, explaining the short delay in punch-down in the SS weld (bottom).

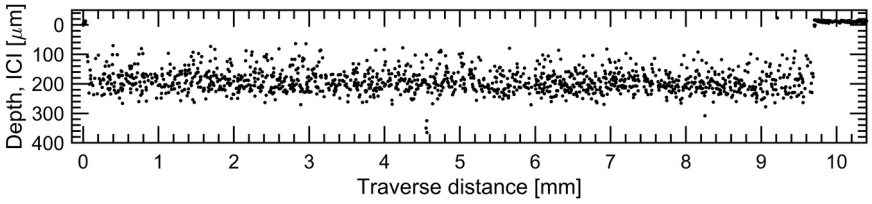

Fig. 3. ICI measured depth profile using maximum intensity tracking (relative to the substrate) from a ~9.5 mm (19 ms laser on-time) long line weld on aluminium 6061, laser parameters: 253 W, 510 mm/s. The weld punch down occurs over ~100 μs at a drilling rate of 2.2 ± 0.4 m/s (Fig. S5) and the mean depth of the weld is 215 ± 1 μm. ICI went dark (insufficient backscattered intensity was collected over the integration time [2]) for 71% of the measurements.

height measurements had a standard deviation of 0.06 μm, with no obvious trends over time. This is well below the axial resolution of the ICI system and can therefore be ignored.

The stability of the ICI optics and sample holder to vibration also needed to be verified. A second set of height measurements were captured from the stationary mirror with the laser off but while

translating the stage. The standard deviation was 0.04 μm, which again can be ignored. This confirms that any coupling of vibrations from the stage into the ICI optics was sufficiently reduced by the vibration-damping pad included between the stage and the chamber floor. Finally, a set of height measurements was captured from a polished (1000 grit) Al6061 substrate mounted in the sample holder and translated with the same motion pattern used in this study. The substrate flatness after polishing was verified by raster scanning the ICI imaging beam to capture the stationary 2D morphology, which was flat to within the axial resolution of the ICI system (6 μm). The height data was linear ($R^2 = 0.87$), indicating there was no significant acceleration or deceleration of the stage during imaging. After subtracting the linear fit to account for tilt of the substrate in the holder, the standard deviation was 2.0 μm. Since the surface roughness for surfaces polished with 1000 grit sandpaper is expected to be < 0.1 μm [38], the majority of this deviation is attributed to jitter or variation in the stage traverse speed and instability of the stage carriage.

2.3. Synchrotron X-ray imaging

The X-ray beam energy was set to 24.4 keV. The imaging system consisted of a LuAG:Ce scintillator, a 10x microscope objective (Mitutoyo NT46–144) that set the resolution and maximum field of view to 2 μm x 2 μm/pixel and 560 μm x 786 μm (at the chosen frame rate) using a Photron FastCam SA-Z 2100 K (Photron Inc., Tokyo, Japan). Frame rate was held constant at 140 kfps with an exposure time of 595 ns. Before writing each track, a set of flat field images was collected with the same number of frames captured *operando* while executing the same motion pattern. The Photron FastCam includes automatic dark-field correction. All acquired radiographs were processed in Matlab 2022a by first applying a moving window flat-field correction. To average over any stage jitter, each radiograph was divided by the median of a window of 25 flat field images:

$$FFC(n) = \frac{I_0(n) - \text{median}(Flat(n-12:n+12))}{\text{median}(Flat(n-12:n+12))}$$

where n is the frame number, $FFC(n)$ is the n^{th} flat-field corrected image, $I_0(n)$ is the corresponding raw image, and $Flat(n)$ is the corresponding flat-field image. The built-in function "imgaussfilt" was then used to Gaussian filter each radiograph, with a standard deviation of 0.5 pixels. To better resolve the keyhole walls and pores, radiograph contrast was enhanced by histogram stretching, saturating the top and bottom 3% of values. To segment the keyhole and extract its depth from each radiograph, we used the image processing algorithm detailed in [6].

Finally, a series of function generators were used to trigger the opening of the slow and fast X-ray shutters at the beamline, stage motion, laser, start of X-ray imaging, and the start of ICI. The synchronization between ICI and X-ray imaging was verified using the laser turn-off. The keyhole collapse observed within one radiograph was simultaneously observed over the corresponding pair of ICI measurements, verifying that the two are synchronized to ± 3.6 μs or better. However, based on typical rise times for function generators it is expected that synchronization is better than 1 μs.

3. Results and discussion

3.1. Comparison of ICI depth profiles for aluminum and stainless steel

To underscore the need for simultaneous X-ray studies, ICI depth-tracking of typical laser bead-on-plate welding (Section A.3) is shown in Fig. 2 for two materials: aluminum alloy 6061 and stainless steel 316 L. The energy densities were chosen to achieve similar keyhole depths for ease of comparison.

The contrasting keyhole dynamics are immediately apparent. Overall, the stainless steel weld achieves a very stable keyhole depth, with a small number of intermediate interfaces attributed to keyhole closure, ejecta, sidewall signals or noise. The small number of these intermediate interfaces should be noted: they account for < 1% of A-lines. Aluminum is markedly different. Punch down is delayed ~3 ms after laser turn on. More importantly, a considerable number of depths shallower than the root are measured (std. dev. 105 μm), and particular deep transients appear every ~mm (e.g., 1.8 ms). This highly irregular behaviour is typical of aluminum welds at Yb-doped laser fiber wavelengths (1070 nm) and its difference from stainless steel is attributed to aluminum's low density (Al ~2380 kg/m^3 vs. Fe ~7030 kg/m^3), low viscosity (Al ~1.3 mPa·s vs. Fe ~6 mPa·s at their respective melting points [39]), and sharp fall-off in absorptivity above the Brewster angle (~86°) [40]. The fact that the welding behaviour is so different is no surprise, but that does not elucidate the cause of these specific measurements (e.g., keyhole collapse, pore formation, ejecta, side wall backscatter).

3.2. Simultaneous synchrotron X-ray and ICI imaging

Similar variations in depth can be seen in ICI depth-tracking for aluminum 6061 bead-on-plate welding using the APS LPBF test rig (Fig. 3) but now we have access to the full 2D cross-section through simultaneous synchrotron X-ray imaging (e.g., Supplementary Movie 1). As mentioned previously, the slow X-ray shutter does not completely open until ~5 ms or ~2.5 mm into the weld meaning only the last 14 ms of Fig. 3 correspond to Supplementary Movie 1. The movie shows that the weld is highly turbulent, as expected based on the ICI depth profile, with repeated sequences of sidewall pinching, partial keyhole collapse and bubble formation. Since ICI and X-ray imaging are synchronised (two ICI measurements for every radiograph), we can now do a detailed point-by-point comparison (Fig. 4). Even with complex and fast keyhole dynamics, there is a strong correlation between ICI and X-ray (0.62). Results are clustered in three main zones. 80% of ICI depth measurements are within 14 μm of the keyhole depth extracted from the corresponding radiograph (dots between solid lines in Fig. 4). This range corresponds roughly to the uncertainty in the depth extracted from

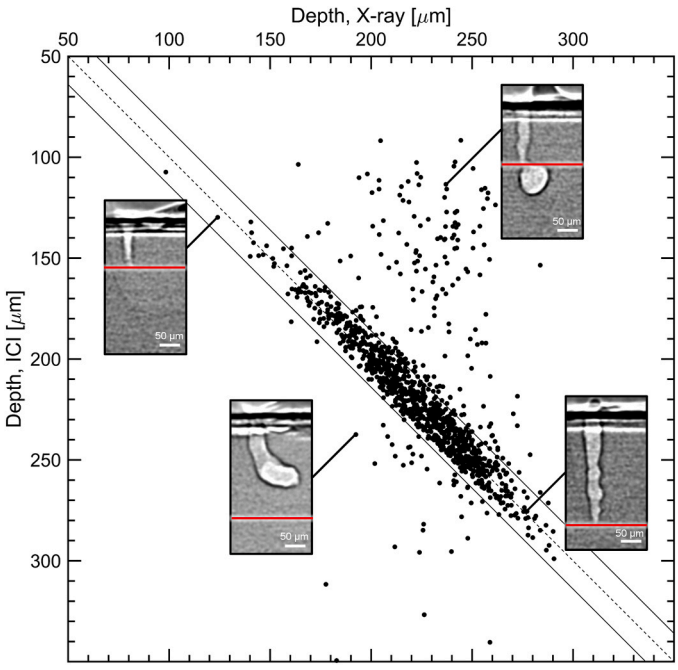

Fig. 4. Depths measured with ICI (maximum intensity tracking) and depth extracted from corresponding radiographs show excellent correlation (Pearson's correlation coefficient: 0.62). 80% of ICI measurements are within 14 μm of radiograph extracted depth (solid black lines). (Insets) Representative radiographs. Red line in inset shows corresponding ICI measured depth.

radiography (8 μm set by the thickness of the high contrast region of the keyhole walls which is typically ~4 pixels) and the ICI axial resolution of 6 μm. Simple keyhole shapes observed by X-ray show excellent agreement between ICI and X-ray for depths ranging from shallow to deep (e.g., radiographs in the top left and bottom right insets of Fig. 4). The red line in the insets indicates the depth measured by ICI during the frame. In each of these cases, only one of the two A-lines acquired during the X-ray frame was above the noise threshold (noise threshold detailed in Section 3.4).

Supplementary material related to this article can be found online at doi:10.1016/j.colsurfa.2023.132032.

Of the cases when ICI and X-ray significantly disagree (20% of all cases), the ICI measured depth is shallower than X-ray 83% of the time (top right zone in Fig. 4). The top right inset shows a typical result and provides a clear explanation for this phenomenon. Imaging light is likely backscattering off the keyhole sidewalls at the point where they are pinching and occluding the keyhole root. The cavity at the keyhole root has a small opening, having almost closed off to form a bubble. This means that any imaging light that does enter the cavity is likely to be trapped—scattered off the cavity walls multiple times until it has been significantly absorbed. Other keyhole geometries that could result in a similar shallow ICI depth measurement are illustrated in Fig. 5b and c. The "wine glass" keyhole shape (Fig. 5b) is typically observed after a partial keyhole collapse. The sudden increase in the energy density at the keyhole root results in rapid drilling and the formation of a high aspect ratio newborn keyhole [41,42]. Humps (Fig. 5c) may also form and travel along the front keyhole wall due to the strong dependence of laser absorptivity on angle of incidence near the Brewster angle [43]. The ICI beam can backscatter off the upward-facing sections of these humps, towards the rear keyhole wall, and out the keyhole opening.

The synchronized radiographs also provide insight into the origin of the ICI depth measurements that are considerably deeper than the keyhole depth extracted from radiography (bottom right corner of Fig. 4). The bottom left inset in Fig. 4 shows a J-shaped keyhole. ICI depth measurements correspond to the optical path length that the imaging light travels. For a J-shaped keyhole, the imaging light can travel a path like that shown in Fig. 5d, resulting in an ICI-measured depth exceeding the true keyhole depth. As mentioned earlier, multiple reflections resulting in a deep ICI measurement like this are rare—only 17% of the outliers (3.4% of all cases). This is related to the number of times the keyhole assumes this shape but this low rate is also attributed to: (1) a higher number of reflections (on average), and therefore more loss of imaging light to absorption, and (2) a lower likelihood that the backscattered imaging light falls within the collection angle of the ICI optics.

Example radiographs of keyhole geometries similar to those depicted in Fig. 5 are shown in Figs. 6–8. Since we have access to the keyhole cross-section, we can further elucidate the connection between shape and ICI-measured path length using ray-tracing. This should also help reveal if some of the discrepancy between the ICI and X-ray depth is caused by fast changes in keyhole morphology over the ICI integration time. That is, if the predominant keyhole morphology during the X-ray integration time of 595 ns differs significantly in depth from the predominant keyhole morphology during the ICI integration time of ~1.5 μs. For example, if the keyhole collapsed shortly after the X-ray integration time.

3.3. Ray-tracing simulations

Based on a similar model developed by Tan et al. [44], we divide the incident ICI imaging light into 10,000 rays and propagate those rays into the keyhole shape extracted from X-ray imaging. The trajectory and intensity of each ray are calculated according to the assumption of linear ray transmission and the law of light reflection and Fresnel absorption at each reflection. Since each radiograph is a 2D projection of the keyhole shape, ray-tracing was limited to 2D. While this introduces an obvious source of error, it was found to mostly affect the predicted backscattered intensity and not depth, suggesting that the keyhole has some circular symmetry. The depth predicted from ray-tracing is even more strongly correlated with the ICI measured depth (0.94 compared to the earlier value of 0.62), with 57% fewer outliers (Fig. S7). Several example cases

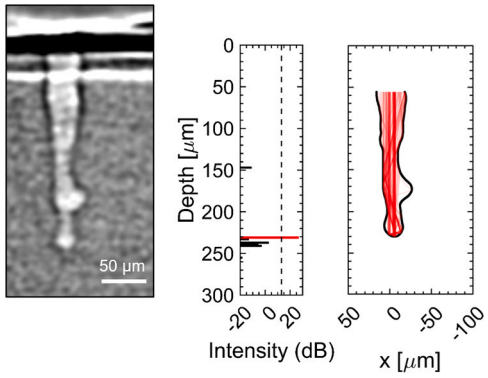

Fig. 6. Ray-tracing results from an example radiograph (left) for which ICI and X-ray agree on the depth. A histogram of the predicted backscattered intensity as a function of depth (middle), binned with the same average bin size as ICI (~2.5 μm), shows a strong peak at the keyhole root. The rays with pathlengths in the maximum intensity bin (right) show mostly direct back reflections off the keyhole root.

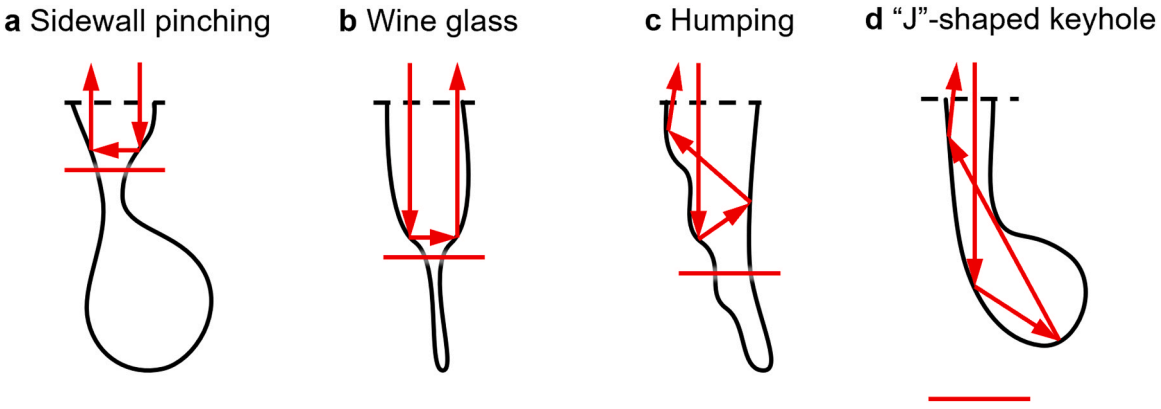

Fig. 5. Schematic diagram of multiple reflection ray trajectories for four characteristic keyhole geometries: sidewall pinching (a), see Fig. 7b; wine glass (b), see Fig. 7a; surface waves (c), see Fig. 6; and root cavity (d), see Fig. 8. The resulting depth measurement is indicated by a solid red line in each case and is shallower than the true keyhole depth in (a)-(c) and deeper than the true keyhole depth in (d).

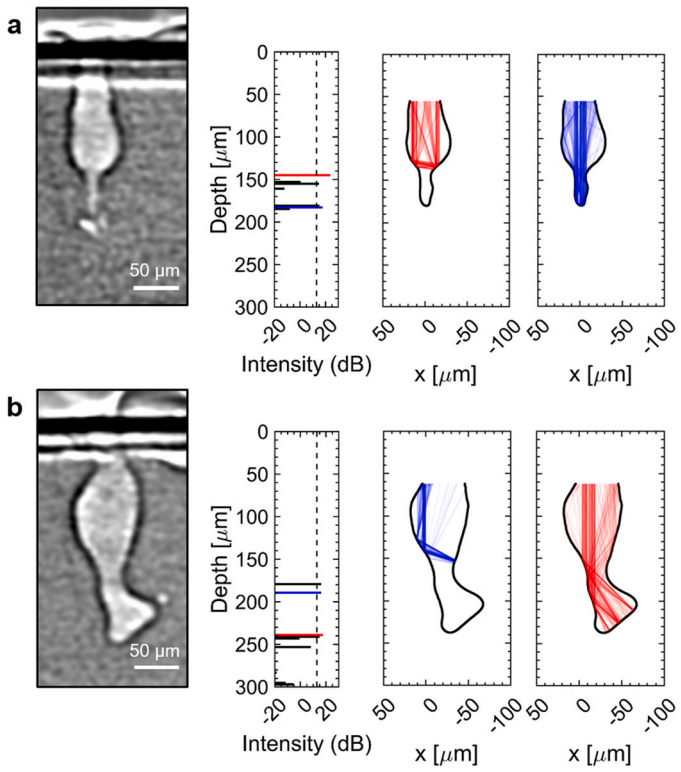

Fig. 7. Ray-tracing results from example radiographs (left) when ray-tracing predicts multiple interfaces above the noise floor. In both cases (a) and (b) one interface is due to side-wall reflections and is shallower than the keyhole root and the other is at the keyhole root. Rays with pathlengths in the maximum intensity bin (brighter of the two interfaces) are shown in red, while rays with pathlengths in the bin for the secondary interface are shown in blue. In (a), ICI and ray-tracing disagree with X-ray, while in (b) all three agree.

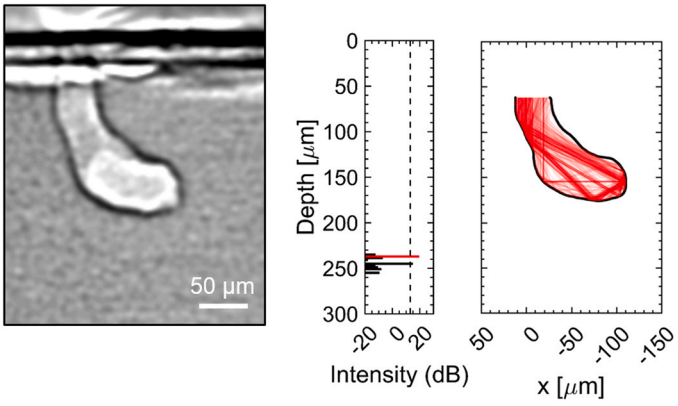

Fig. 8. Ray-tracing results from an example radiograph (left) for which the ICI measured depth is significantly deeper than the depth extracted from X-ray imaging. A histogram of the predicted backscattered intensity as a function of depth (middle), binned with the same average bin size as ICI (~2.5 μm), shows a peak at a depth of 240 μm. This is 62 μm below the root of the keyhole (178 μm) and a result of multiple reflections (right).

are shown in Figs. 6–8, including each of the keyhole geometries predicted to result in multiple reflections shown in Fig. 5. Extracting accurate information from these outliers is critical for tracking fast keyhole dynamics like bubble formation.

Despite deviating from the true keyhole depth, information can still be extracted from ICI measurements resulting from multiple reflections. Pinching of the keyhole walls may foreshadow keyhole collapse, and the formation of new keyholes or excessive humping on the keyhole walls may indicate instability in the process (Section 3.5). A focus of future work will be extracting information about the 2D keyhole geometry from each A-line, rather than just a single value for depth. For example, a machine learning approach like that described in ref. [45] could be used, except with keyhole geometries from radiography as a training dataset.

3.4. *Effect of noise thresholding and decimation on ICI tracking accuracy*

As mentioned previously, each ICI measurement or "A-line" includes backscattered intensity as a function of depth. To extract a single depth value from each A-line, a threshold is first applied to avoid errors due to background noise. Typically, the threshold is based on measurements without an interface and selected to limit error rates to $< 1\%$ [46]. While setting a high threshold lowers the probability of false interfaces, it also discards true interfaces and reduces the effective acquisition rate. Past work could not quantify the relationship between effective acquisition rate and noise threshold without verification of the measurements near the noise floor. With synchronized radiography, we can now demonstrate the importance of the noise threshold (Fig. 9). Increasing the threshold from 13 dB (e.g. to 20 dB) would increase the correlation with X-ray (from 0.62 to 0.70) but at the expense of bright A-lines (from 29% to 22%). Decreasing the threshold (e.g. to 10 dB) would have the opposite effect, increasing the number of bright A-lines (from 29% to 35%) but at the expense of significantly worse correlation with X-ray (from 0.62 to 0.36). While this relationship is somewhat specific to the imaging system and processing conditions used here, the general trend is likely true across different systems and welds/LPBF tracks. The specific threshold value selected will depend on the application and the need for either high-speed (i.e., low threshold) or high-fidelity (high threshold) depth-tracking.

Thresholding is the first step of data processing. Different depth-tracking strategies can then be used to extract the depth profile from a single or series of A-line images. Most often, the depth pixel with the maximum intensity is identified as the depth. However, in cases when sufficient ICI signal is collected from both side walls and the keyhole root, termed "multiple interfaces", it is more accurate to track the deepest pixel above the noise threshold, see Fig. S6. This was previously shown to improve the agreement between *operando* ICI and *ex situ* X-ray [47] of deep-penetration welding but found to be minimal for the depth profile shown in Fig. 3 (correlation coefficient increased from 0.62 to 0.64). Multiple interfaces were observed in only ~2% of bright A-lines. Furthermore, more than half of the multiple interfaces were for cases when ICI and X-ray already agreed and maximum intensity and deepest interface tracking extracted the same depth. For the remaining A-lines with multiple interfaces, $> 80\%$ benefit from changing to deepest interface tracking (maximum intensity depth shallower than X-ray). This supports the hypothesis that deepest-interface tracking could improve tracking accuracy for depth profiles with a higher percentage of multiple interfaces, e.g., from deep-penetration welding, but only minimally.

The last data processing step is decimation. The sample rate of the extracted depth profile can be reduced by again selecting the depth pixel with maximum intensity but over segments of A-lines (the number of A-lines in each segment corresponds to the decimation factor). This is useful since in many cases ICI oversamples depth. For example, for the same acquisition rate of 280 kHz but at a scan speed of 10 mm/s more typical of DED, the laser only moves ~0.04 μm in between successive ICI depth measurements. The effect of decimation on correlation with simultaneous X-ray imaging is shown in Fig. 10. No decimation was performed on the X-ray depth data to calculate the correlation values. Rather, each whole decimation window in the ICI depth data was assigned the same depth value. Increasing the decimation factor (up to approximately 20) increases the correlation from 0.62 to 0.79 but with the obvious reduction in effective imaging rate. A decimation factor of 20 also resulted in the complete removal of dark A-lines (when ICI peak signal is below the threshold).

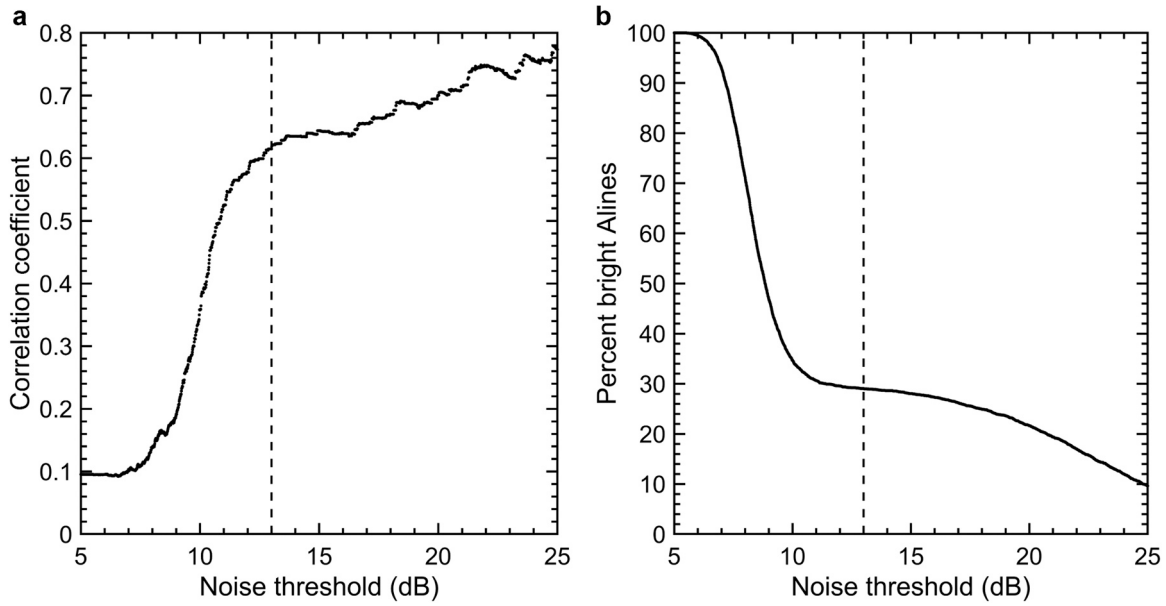

Fig. 9. Correlation between depth measured using ICI and keyhole depth from X-ray imaging, as a function of the noise floor applied to ICI data. Dashed line corresponds to a threshold of 13 dB used in previous figures.

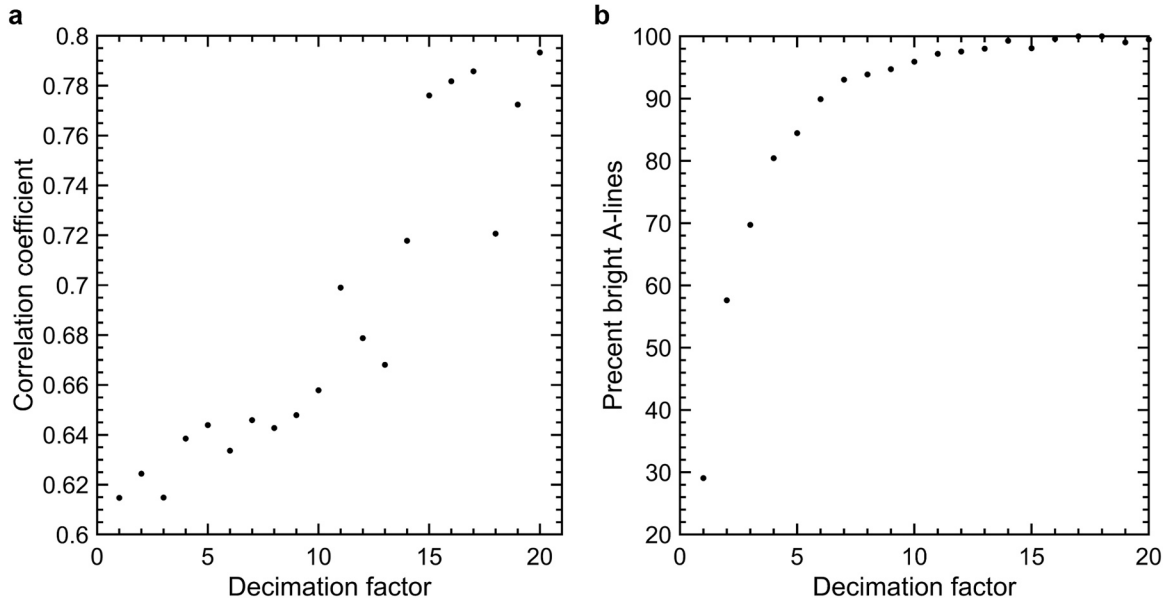

Fig. 10. Correlation between depth measured using ICI and keyhole depth from X-ray imaging, as a function of the decimation factor applied to the ICI data.

As shown in Fig. 10b, the number of bright A-lines almost doubles after decimating by a factor of 2. This is because most bright ICI A-lines were isolated (>80%), i.e. surrounded by dark A-lines. The statistics of bright and dark A-lines will be a point of further investigation. Simultaneous radiography can also be used to understand the dependence of A-line intensity on 2D keyhole morphology. This is useful for optimizing the imaging beam location(s) relative to the laser to maximize intensity. For high-speed laser welding and LPBF, the tilt of the front keyhole wall increases with scan speed and results in an offset of the keyhole root from the laser beam [5]. If the ICI beam is positioned along the tilted front keyhole wall it is likely to experience multiple reflections deeper into the keyhole, reducing backscattered intensity by absorption and redirection of the imaging beam outside the ICI system's collection angle. The traditional coaxial alignment of ICI to the laser beam is no longer optimal under these process conditions.

3.5. Depth signatures of bubble formation

Pore formation is very important for final part structural integrity, and the dynamics of bubble generation have been examined in several high-speed X-ray studies [15,25,48]. Zhao et al. [42] used ultrahigh speed X-ray imaging (>1 MHz) of laser welding and LPBF of Ti-6Al-4 V to reveal a sequence of keyhole events leading to bubble formation: (1) formation of a letter J-shaped keyhole, (2) collapse of the keyhole side walls, and (3) formation of a bubble and "newborn" keyhole. The whole sequence was observed to last < 5 μs, with the keyhole collapse at > 10 m/s (horizontal). The keyhole depth profile extracted from *operando* radiographs includes a step decrease once the sidewalls impinge on each other to complete the keyhole collapse followed by a rapid expansion and drilling of the newborn keyhole (>10 m/s), which plateaus at the steady-state depth. Interestingly, the authors also point out

that the rapid expansion of the newborn keyhole is due (in part) to phase explosion [49], which results in roughened and wrinkled keyhole walls from the impact of liquid metal droplets. Considering the dramatic changes to morphology present in bubble formation, it is suggestive that these signatures may be evident in simple ICI data. To be able to see bubbles as they form would be extremely useful but we recognize that the time scales resolved in previous X-ray studies show that bubble generation dynamics will be at the top end of the ICI capabilities used here.

Three example sequences of bubble formation events are found in the radiographs (Fig. 11) and shown with corresponding ICI-measured depths. As discussed above, J-shaped keyholes yield dark ICI measurements as shown in sequences in Fig. 11a and b. In Fig. 11a, ICI recorded a bright measurement of the newborn keyhole shortly after its formation (t_0 +14 μs, where t_0 is defined as the time of the initial frame), and after its rapid expansion (t_0 +21 μs). In Fig. 11b, a keyhole collapse likely occurred between t_0 and $t_0 + 7$ μs and was not resolved with either X-ray or ICI. A more gradual pull-up is observed over the following three frames (t_0 +7 μs to t_0 +21 μs). This is likely a result of an acoustic shock wave induced by keyhole-pore interactions at $t_0 + 7$ μs, termed "pore rebound" [42]. Following this pull-up, rapid drilling and expansion again occur at the needle-like keyhole root resulting in the much larger and deeper keyhole at $t_0 + 28$ μs. In Fig. 11c, while no J-shaped keyhole is observed, sidewall pinching, and keyhole collapse are well resolved by ICI from t_0 to $t_0 + 7$ μs. The bubble pinched off from the keyhole root is then observed to split twice over the subsequent ~30 μs (t_0 +14 to t_0 +21 μs and t_0 +35 μs). These interactions again induce acoustic waves driving sharp changes in keyhole depth.

To locally detect pore generation with ICI, the changes in depth due to keyhole collapse and expansion of the newborn keyhole need to be resolved and differentiated from steady-state fluctuations. A challenge with testing this hypothesis is that ICI imaging will need to be continuous throughout the sequence of depth changes. As discussed above, this will require decimation to reduce the impact of dark A-lines, but excessive decimation will obscure the sudden changes in morphology. As an initial step towards on-the-fly detection, the bubble formation events observed from radiography were correlated with the depth measured using ICI (Fig. 3).

While ICI is nominally at 280 kHz in this work, typical numbers of dark measurements lower the effective acquisition rate to < 100 kHz. Assuming dark measurements are regular, the effective acquisition rate in this study is 81 kHz (71% dark measurements) but to locally detect pore formation *operando* ICI data will need to be sectioned. The irregular timing of dark measurements then becomes more apparent, with effective acquisition rates varying from 66 to 97 kHz over 1 ms segments (280 ICI measurements) and 40–130 kHz over 100 μs segments (28 ICI measurements). The likelihood of a bright ICI interface is expected to be higher for the newborn keyhole than the J-shaped keyhole due to a smaller average number of multiple reflections. The roughness of the newborn keyhole walls due to phase explosion may also diffusely scatter the ICI beam, making it more likely that the backscattered light falls within the acceptance angle of the ICI imaging system.

To calculate the correlation values listed in Table 2, the ICI depth profile was first decimated by a factor of two using the maximum intensity method (Sect. 3.4). This matched the acquisition rate of X-ray and reduced the number of dark measurements (from 71% to 48%). Only considering the bubble formation events when the corresponding depth measurement was bright (63%), the correlation coefficient was

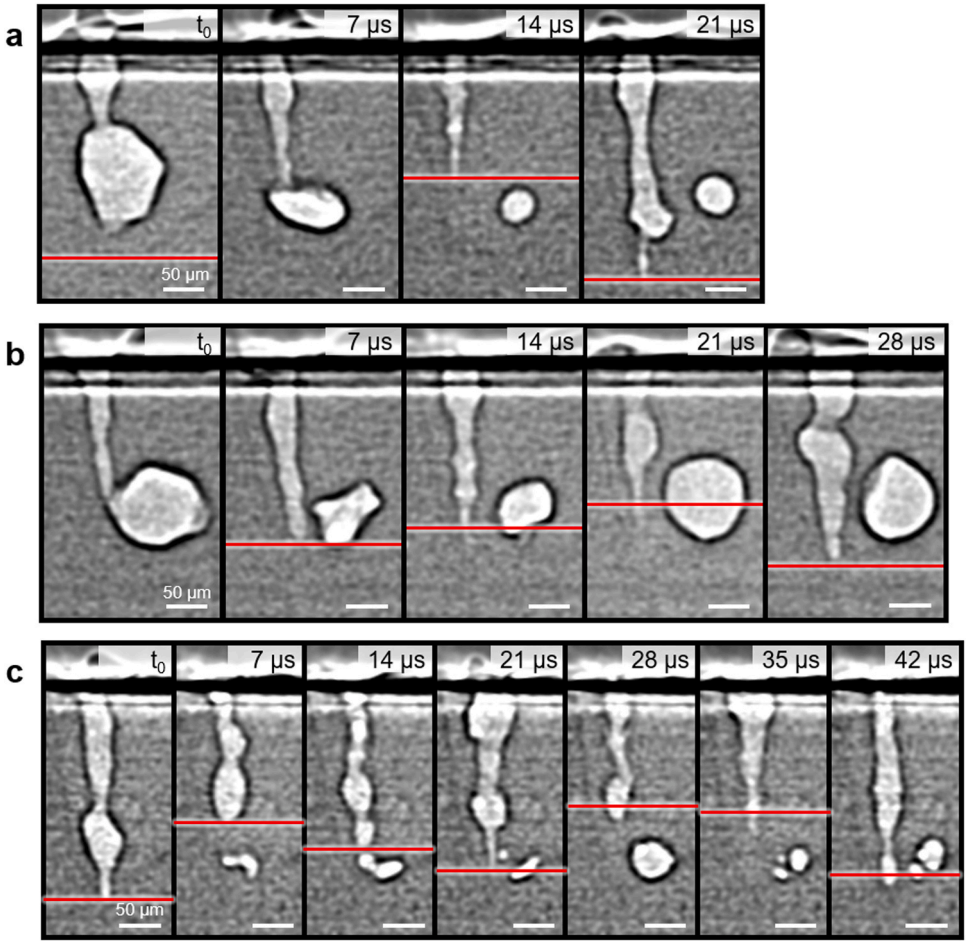

Fig. 11. Three example pore generation sequences simultaneously resolved with synchrotron X-ray radiography and ICI. Red line is at ICI measured depth.

Table 2
Pearson's correlation coefficient for correlation between depth, its first difference, and bubble formation events. ICI depth is decimated by a factor of four using the maximum intensity method. Since the variable for bubble formation events is binary, Pearson's correlation coefficient is equivalent to the point-biserial correlation coefficient. Negative values indicate a bubble formation event is correlated with a lesser depth or lesser/negative first difference in depth.

	Pearson's correlation coefficient with bubble formation events (P-values << 0.001)
Depth, X-ray	-0.30
First difference in depth, X-ray	-0.35
Depth, ICI	-0.17
First difference in depth, ICI	-0.26

found to be − 0.32. The correlation is negative because the keyhole is typically shallower than average when a bubble forms due to partial keyhole collapse.

Too few of the first differences in depth corresponding to bubble formation events were bright after decimating by a factor of two (26%) to make significant conclusions from a correlation. Decimating instead by a factor of four infilled all the dark measurements corresponding to bubble formation events but was found to weaken the correlation with depth to a coefficient of − 0.17. This likely results from the fast dynamics of the process at or above the Nyquist frequency, which is 35 kHz after decimating by a factor of four. A slightly stronger correlation was found with the first difference in depth ($d_{n+1} - d_n$) (−0.26). This is likely due to the brevity of keyhole spiking and collapse phenomena linked to bubble formation (<15 μs, <4 ICI measurements) and the high standard deviation in depth (37 μm).

The correlations listed in Table 2 are all significant (P-values << 0.001) and suggest that it may be possible to find features from short windows of ICI-measured depth that sufficiently separate bubble formation events, allowing for classification and detection. Due to the number of dark measurements and brevity of bubble formation phenomena, these features will be sensitive to the decimation strategy. Bubbles that form pores (here, 21%) or the largest bubbles may also separate more in the selected feature space.

To increase the likelihood of success in feature selection and classification, higher ICI acquisition rates could be used to better resolve keyhole spiking and collapse. This could be achieved by, for example, multiplexing several ICI systems (588 kHz in ref. [50]) or changing from the spectral-domain system used here to a swept-source system capable of > 1 MHz nominal acquisition rates [51]. Based on the process conditions (somewhat increased wobble from stage relative to galvanometer scanner, high O_2 atmosphere), and keyhole dynamics observed in Supplementary Movie 1, the laser weld presented in this study was in pore-generation mode. Over the final 14 ms (~7 mm) of the weld (Fig. 3, Supplementary Movie 1) that was captured with X-ray, 18 pores were generated with an average time spacing of ~0.78 ms (~0.4 mm). This is at least an order of magnitude higher than in ref. [24] which classified (pore vs. no pore) *operando* AE data segments with a minimum duration of 2.5 ms. Their classifier would likely register pores for the entirety of the weld studied here. If process parameters were optimized to minimize pore formation, the resulting depth profile measured with ICI could be easily distinguished from the one presented here. This is certainly the case when comparing laser weld depth profiles across different materials, with far less pore formation in steel than aluminum under otherwise similar conditions for example. Future work will include capturing similar *operando* datasets but in pore-generation *and* stable modes for the same material.

4. Conclusions

High-speed (280 kHz) depth measurements captured using inline coherent imaging (ICI) during laser keyhole welding are dynamically verified by synchrotron X-ray imaging for the first time. Even for a turbulent laser weld on aluminum alloy 6061 with violent changes in keyhole morphology and pores every ~400 μm, the depth measured from the keyhole using ICI agrees well with the keyhole depth extracted from synchrotron radiography (>80% within ± 14 μm).

Synchrotron X-ray imaging provides new insights into outliers—when the ICI depth measurement deviates significantly from X-ray. It also elucidates the effect of key data processing steps, like noise thresholding and decimation, on the effective acquisition rate and fidelity of ICI. Sidewall pinching, wine glass-shaped keyholes, and humping along the front keyhole wall were observed in radiographs corresponding to outliers in the ICI depth profile when it was significantly shallower than X-ray (> 14 μm). For outliers when the ICI measured depth was significantly deeper than X-ray, J-shaped keyholes were often observed, a potential precursor shape to bubble formation. To better understand these outliers, the 2D keyhole shape was extracted from corresponding radiographs and input into a ray-tracing simulation. For 57% of the outliers, ray-tracing predicted multiple reflections of the imaging beam resulting in the same depth measurement as ICI (within uncertainty). The depth profile predicted from ray-tracing was strongly correlated with ICI (0.94).

Finally, fast changes in depth during bubble formation due to partial keyhole collapse and redrilling of the keyhole are resolved by ICI in several instances. ICI measured depth (d) as well as its first difference ($d_{n+1} - d_n$) are found to be weakly correlated with bubble formation events (0.17–0.26). This suggests that through proper feature extraction, including sectioning of the ICI data, bubble formation during laser keyhole welding and LPBF should be detectable on-the-fly using ICI.

CRediT authorship contribution statement

Tristan G. Fleming: Conceptualization, Methodology, Formal analysis, Investigation, Writing – original draft, Writing – review & editing, Visualization, Project administration. **Samuel J. Clark:** Methodology, Investigation, Writing – review & editing. **Xianqiang Fan:** Investigation. **Kamel Fezzaa:** Investigation. **Chu Lun Alex Leung:** Conceptualization, Methodology, Writing – review & editing, Project administration, Funding acquisition. **Peter D. Lee:** Conceptualization, Methodology, Writing – review & editing, Project administration, Funding acquisition. **James M. Fraser:** Conceptualization, Methodology, Writing – review & editing, Project administration, Funding acquisition.

Declaration of Competing Interest

The authors declare the following financial interests/personal relationships which may be considered as potential competing interests: IPG Photonics (Canada) Inc. has commercialised inline coherent imaging. They are at arms-length to Queen's University. During the course of this work, authors were neither employees nor owners of this company.

Data availability

Data will be made available on request.

Acknowledgements

PDL, CLAL and TF are grateful for the support from MAPP: EPSRC Future Manufacturing Hub in Manufacture using Advanced Powder Processes (EP/P006566/1), EPSRC Impact Acceleration Account (EP/R511638/1), Manufacturing by Design (EP/W003333/1) and Made Smarter Innovation – Materials Made Smarter Research Centre (EP/V061798/1), EPSRC International Centre to Centre (IC2C) Collaboration on Manufacturing by Design (EP/W003333/1). PDL is funded by the support from the Royal Academy of Engineering Chair in Emerging

Technologies (CiET1819/10); CLAL is funded by Data-driven, Reliable, and Effective Additive Manufacturing using multi-BEAM technologies (EP/W037483/1). TF and JMF acknowledge the support of the Natural Sciences and Engineering Research Council of Canada (NSERC), [funding reference number 5011063–2018], the NSERC Collaborative Research and Training Experience program [511093–2018], the Canadian Foundation for Innovation, and the Ontario Centres of Excellence. This research used resources of the Advanced Photon Source, a U.S. Department of Energy (DOE) Office of Science User Facility, operated for the DOE Office of Science by Argonne National Laboratory under Contract No. DE-AC02–06CH11357. We thank the Advanced Photon Source for providing the beamtime (73825). Many thanks to SJC, KF and other beamline staff at the Advanced Photon Source as well as team members from the Materials, Structure and Manufacturing group at Harwell (MSM@H) for their assistance in preparation for and during the beamtime: Anna Getley and Xianqiang Fan. The authors are also grateful to Daniel Cliffe (Parker Hannifin Corporation) and James Sanker (Shelley Automation) for their assistance in configuring the linear motion stage.

Appendix A. Supporting information

Supplementary data associated with this article can be found in the online version at doi:10.1016/j.addma.2023.103798.

References

[1] P.J.L. Webster, L.G. Wright, Y. Ji, C.M. Galbraith, A.W. Kinross, C. Van Vlack, J. M. Fraser, Automatic laser welding and milling with *in situ* inline coherent imaging, Opt. Lett. 39 (2014) 6217, https://doi.org/10.1364/OL.39.006217.

[2] J.A. Kanko, A.P. Sibley, J.M. Fraser, *In situ* morphology-based defect detection of selective laser melting through inline coherent imaging, J. Mater. Process. Technol. 231 (2016) 488–500, https://doi.org/10.1016/j.jmatprotec.2015.12.024.

[3] D. You, X. Gao, S. Katayama, Detection of imperfection formation in disk laser welding using multiple on-line measurements, J. Mater. Process. Technol. 219 (2015) 209–220, https://doi.org/10.1016/J.JMATPROTEC.2014.12.025.

[4] T. Vilaro, C. Colin, J.D. Bartout, As-fabricated and heat-treated microstructures of the Ti-6Al-4V alloy processed by selective laser melting, Metall. Mater. Trans. A 42 (2011) 3190–3199, https://doi.org/10.1007/S11661-011-0731-Y.

[5] R. Cunningham, C. Zhao, N. Parab, C. Kantzos, J. Pauza, K. Fezzaa, T. Sun, A. D. Rollett, Keyhole threshold and morphology in laser melting revealed by ultrahigh-speed X-ray imaging, Science 363 (2019) 849–852, https://doi.org/10.1126/science.aav4687.

[6] Y. Huang, T.G. Fleming, S.J. Clark, S. Marussi, K. Fezzaa, J. Thiyagalingam, C.L. A. Leung, P.D. Lee, Keyhole fluctuation and pore formation mechanisms during laser powder bed fusion additive manufacturing, Nat. Commun. 13 (2022) 1–11, https://doi.org/10.1038/s41467-022-28694-x.

[7] N. Kumar, I. Masters, A. Das, In-depth evaluation of laser-welded similar and dissimilar material tab-to-busbar electrical interconnects for electric vehicle battery pack, J. Manuf. Proc. 70 (2021) 78–96, https://doi.org/10.1016/j.jmapro.2021.08.025.

[8] A. Das, D. Li, D. Williams, D. Greenwood, Joining technologies for automotive battery systems manufacturing, World Electr. Veh. J. 9 (2018) 22, https://doi.org/10.3390/WEVJ9020022.

[9] T.R. Allen, W. Huang, J.R. Tanner, W. Tan, J.M. Fraser, B.J. Simonds, Energy-coupling mechanisms revealed through simultaneous keyhole depth and absorptance measurements during laser-metal processing, Phys. Rev. Appl. 13 (2020), 064070, https://doi.org/10.1103/PHYSREVAPPLIED.13.064070.

[10] M. Sokolov, P. Franciosa, R. Al Botros, D. Ceglarek, Keyhole mapping to enable closed-loop weld penetration depth control for remote laser welding of aluminum components using optical coherence tomography, J. Laser Appl. 32 (2020), 032004, https://doi.org/10.2351/7.0000086.

[11] B. Sander, M. Larsen, L. Thrane, J.L. Hougaard, T.M. Jørgensen, Enhanced optical coherence tomography imaging by multiple scan averaging, Br. J. Ophthalmol. 89 (2005) 207–212, https://doi.org/10.1136/BJO.2004.045989.

[12] B. Qiu, Z. Huang, X. Liu, X. Meng, Y. You, G. Liu, K. Yang, A. Maier, Q. Ren, Y. Lu, Noise reduction in optical coherence tomography images using a deep neural network with perceptually-sensitive loss function, Biomed. Opt. Express 11 (2020) 817, https://doi.org/10.1364/BOE.379551.

[13] A.E. Desjardins, A. Bilenca, A. Ozcan, B.E. Bouma, G.J. Tearney, Speckle reduction in optical coherence tomography images using digital filtering, JOSA A 24 (2007) 1901–1910, https://doi.org/10.1364/JOSAA.24.001901.

[14] M. Boley, F. Fetzer, R. Weber, T. Graf, Statistical evaluation method to determine the laser welding depth by optical coherence tomography, Opt. Lasers Eng. 119 (2019) 56–64, https://doi.org/10.1016/J.OPTLASENG.2019.03.014.

[15] A.A. Martin, N.P. Calta, S.A. Khairallah, J. Wang, P.J. Depond, A.Y. Fong, V. Thampy, G.M. Guss, A.M. Kiss, K.H. Stone, C.J. Tassone, J.N. Weker, M. F. Toney, T. van Buuren, M.J. Matthews, Dynamics of pore formation during laser powder bed fusion additive manufacturing, Nat. Commun. 10 (2019), 1987, https://doi.org/10.1038/s41467-019-10009-2.

[16] M. Schmoeller, C. Stadter, S. Liebl, M.F. Zaeh, Inline weld depth measurement for high brilliance laser beam sources using optical coherence tomography, J. Laser Appl. 31 (2019), 022409, https://doi.org/10.2351/1.5096104.

[17] J.M. Schmitt, S.H. Xiang, K.M. Yung, Speckle in optical coherence tomography, J. Biomed. Opt. 4 (1999) 95–105, https://doi.org/10.1117/1.429925.

[18] N.H. Paulson, B. Gould, S.J. Wolff, M. Stan, A.C. Greco, Correlations between thermal history and keyhole porosity in laser powder bed fusion, Addit. Manuf. 34 (2020), 101213, https://doi.org/10.1016/J.ADDMA.2020.101213.

[19] S.A. Khairallah, A.T. Anderson, A. Rubenchik, W.E. King, Laser powder-bed fusion additive manufacturing: Physics of complex melt flow and formation mechanisms of pores, spatter, and denudation zones, Acta Mater. 108 (2016) 36–45, https://doi.org/10.1016/J.ACTAMAT.2016.02.014.

[20] A. Otto, R.G. Vázquez, U. Hartel, S. Mosbah, Numerical analysis of process dynamics in laser welding of Al and Cu, Procedia CIRP 74 (2018) 691–695, https://doi.org/10.1016/J.PROCIR.2018.08.040.

[21] F. Fetzer, H. Hu, P. Berger, R. Weber, P. Eberhard, T. Graf, Fundamental investigations on the spiking mechanism by means of laser beam welding of ice, J. Laser Appl. 30 (2018), 012009, https://doi.org/10.2351/1.4986641.

[22] K. Wasmer, T. Le-Quang, B. Meylan, F. Vakili-Farahani, M.P. Olbinado, A. Rack, S. A. Shevchik, Laser processing quality monitoring by combining acoustic emission and machine learning: a high-speed X-ray imaging approach, Procedia CIRP 74 (2018) 654–658, https://doi.org/10.1016/J.PROCIR.2018.08.054.

[23] S. Shevchik, T. Le-Quang, B. Meylan, F.Vakili Farahani, M.P. Olbinado, A. Rack, G. Masinelli, C. Leinenbach, K. Wasmer, Supervised deep learning for real-time quality monitoring of laser welding with X-ray radiographic guidance, Sci. Rep. 10 (2020) 10, https://doi.org/10.1038/s41598-020-60294-x.

[24] J.R. Tempelman, A.J. Wachtor, E.B. Flynn, P.J. Depond, J.B. Forien, G.M. Guss, N. P. Calta, M.J. Matthews, Detection of keyhole pore formations in laser powder-bed fusion using acoustic process monitoring measurements, Addit. Manuf. 55 (2022), 102735, https://doi.org/10.1016/J.ADDMA.2022.102735.

[25] C.L.A. Leung, S. Marussi, R.C. Atwood, M. Towrie, P.J. Withers, P.D. Lee, *In situ* X-ray imaging of defect and molten pool dynamics in laser additive manufacturing, Nat. Commun. 9 (2018), 1355, https://doi.org/10.1038/s41467-018-03734-7.

[26] S.A. Khairallah, T. Sun, B.J. Simonds, Onset of periodic oscillations as a precursor of a transition to pore-generating turbulence in laser melting, Addit. Manuf. Lett. 1 (2021), 100002, https://doi.org/10.1016/J.ADDLET.2021.100002.

[27] N.D. Parab, C. Zhao, R. Cunningham, L.I. Escano, K. Fezzaa, W. Everhart, A. D. Rollett, L. Chen, T. Sun, Ultrafast X-ray imaging of laser–metal additive manufacturing processes, J. Synchrotron Radiat. 25 (2018) 1467–1477, https://doi.org/10.1107/S1600577518009554.

[28] IPG Photonics, "YLM and YLR-1070 Series: YLR-AC 100–700 W Optical Characteristics." ⟨https://www.ipgphotonics.com/en/products/lasers/mid-power-cw-fiber-lasers/1-micron/ylm-and-ylr⟩ (accessed Aug. 02, 2022).

[29] W.E. King, H.D. Barth, V.M. Castillo, G.F. Gallegos, J.W. Gibbs, D.E. Hahn, C. Kamath, A.M. Rubenchik, Observation of keyhole-mode laser melting in laser powder-bed fusion additive manufacturing, J. Mater. Process. Technol. 214 (2014) 2915–2925, https://doi.org/10.1016/j.jmatprotec.2014.06.005.

[30] J. Ye, S.A. Khairallah, A.M. Rubenchik, M.F. Crumb, G.M. Guss, J. Belak, M. J. Matthews, Energy coupling mechanisms and scaling behavior associated with laser powder bed fusion additive manufacturing, Adv. Eng. Mater. 21 (2019), 1900185, https://doi.org/10.1002/adem.201900185.

[31] S.Z. Uddin, L.E. Murr, C.A. Terrazas, P. Morton, D.A. Roberson, R.B. Wicker, Processing and characterization of crack-free aluminum 6061 using high-termperature heating in laser powder bed fusion additive manufacturing, Addit. Manuf. 22 (2018) 405–415, https://doi.org/10.1016/j.addma.2018.05.04.

[32] E. Cicală, G. Duffet, H. Andrzejewski, D. Grevey, S. Ignat, Hot cracking in Al–Mg–Si alloy laser welding – operating parameters and their effects, Mater. Sci. Eng. A. 395 (2005) 1–9, https://doi.org/10.1016/J.MSEA.2004.11.026.

[33] N.T. Aboulkhair, N.M. Everitt, I. Ashcroft, C. Tuck, Reducing porosity in AlSi10Mg parts processed by selective laser melting, Addit. Manuf. 1 (2014) 77–86, https://doi.org/10.1016/j.addma.2014.08.001.

[34] I. Bitharas, N. Parab, C. Zhao, T. Sun, A.D. Rollett, A.J. Moore, The interplay between vapour, liquid, and solid phases in laser powder bed fusion, Nat. Commun. 13 (2022), 2959, https://doi.org/10.1038/S41467-022-30667-Z.

[35] T.G. Fleming, S.G.L. Nestor, T.R. Allen, M.A. Boukhaled, N.J. Smith, J.M. Fraser, Tracking and controlling the morphology evolution of 3D powder-bed fusion *in situ* using inline coherent imaging, Addit. Manuf. 32 (2020), 100978, https://doi.org/10.1016/j.addma.2019.100978.

[36] P.J.L. Webster, L.G. Wright, K.D. Mortimer, B.Y. Leung, J.X.Z. Yu, J.M. Fraser, Automatic real-time guidance of laser machining with inline coherent imaging, J. Laser Appl. 23 (2011), 022001, https://doi.org/10.2351/1.3567955.

[37] W. Drexler, J.G. Fujimoto, Optical Coherence Tomography, Springer,, Berlin, Heidelberg, 2008.

[38] The European Stainless Steel Development Association, Roughness measurements of stainless steel surfaces, Brussels, 2014.

[39] Y. Huang, T.G. Fleming, S.J. Clark, S. Marussi, K. Fezzaa, J. Thiyagalingam, C.L. A. Leung, P.D. Lee, Keyhole fluctuation and pore formation mechanisms during laser powder bed fusion additive manufacturing, Nat. Commun. 13 (2022) 1–11, https://doi.org/10.1038/s41467-022-28694-x.

[40] A.T. Dinsdale, P.N. Quested, The viscosity of aluminium and its alloys-A review of data and models, J. Mater. Sci. Proc. 39 (2004) 7221–7228, https://doi.org/10.1023/B:JMSC.0000048735.50256.96.

[41] A.F.H. Kaplan, Fresnel absorption of 1 μm- and 10 μm-laser beams at the keyhole wall during laser beam welding: Comparison between smooth and wavy surfaces,

Appl. Surf. Sci. 258 (2012) 3354–3363, https://doi.org/10.1016/j.apsusc.2011.08.086.
[42] C. Zhao, N.D. Parab, X. Li, K. Fezzaa, W. Tan, A.D. Rollett, T. Sun, Critical instability at moving keyhole tip generates porosity in laser melting, Science 370 (2020) 1080–1086, https://doi.org/10.1126/SCIENCE.ABD1587.
[43] A.F.H. Kaplan, R.S. Matti, Absorption peaks depending on topology of the keyhole front and wavelength, J. Laser Appl. 27 (2015), S29012, https://doi.org/10.2351/1.4906469.
[44] W. Tan, N.S. Bailey, Y.C. Shin, Investigation of keyhole plume and molten pool based on a three-dimensional dynamic model with sharp interface formulation, J. Phys. D. Appl. Phys. 46 (2013), 055501, https://doi.org/10.1088/0022-3727/46/5/055501.
[45] C. Stadter, M.K. Kick, M. Schmoeller, M.F. Zaeh, Correlation analysis between the beam propagation and the vapor capillary geometry by machine learning, Procedia CIRP 94 (2020) 742–747, https://doi.org/10.1016/J.PROCIR.2020.09.138.
[46] T.J.H. Krause, T.R. Allen, J.M. Fraser, Self-witnessing coherent imaging for artifact removal and noise filtering, Opt. Lasers Eng. 151 (2022), 106936, https://doi.org/10.1016/J.OPTLASENG.2021.106936.
[47] J.J. Blecher, C.M. Galbraith, C. Van Vlack, T.A. Palmer, J.M. Fraser, P.J.L. Webster, Real time monitoring of laser beam welding keyhole depth by laser interferometry, Sci. Tech. Weld. Join. 19 (2014) 560–564, https://doi.org/10.1179/1362171814Y.0000000225.
[48] A.A. Martin, N.P. Calta, J.A. Hammons, S.A. Khairallah, M.H. Nielsen, R. M. Shuttlesworth, N. Sinclair, M.J. Matthews, J.R. Jeffries, T.M. Willey, J.R.I. Lee, Ultrafast dynamics of laser-metal interactions in additive manufacturing alloys captured by *in situ* X-ray imaging, Mater. Today Adv. 1 (2019), 100002, https://doi.org/10.1016/j.mtadv.2019.01.001.
[49] J. Ramirez-San-Juan, E. Rodriguez-Aboytes, A.E. Martinez-Canton, O. Baldovino-Pantaleon, A. Robledo-Martinez, N. Korneev, R. Ramos-Garcia, Time-resolved analysis of cavitation induced by CW lasers in absorbing liquids, Opt. Express 18 (2010) 8735–8742, https://doi.org/10.1364/OE.18.008735.
[50] C.M. Galbraith, Inline coherent imaging of laser keyhole welding, M.Sc. Thesis. Queen's University Kingston, 2015.
[51] W. Drexler, M. Liu, A. Kumar, T. Kamali, A. Unterhuber, R.A. Leitgeb, Optical coherence tomography today: speed, contrast, and multimodality, J. Biomed. Opt. 19 (2014), 071412, https://doi.org/10.1117/1.JBO.19.7.071412.